Numerical simulation of optical control for a soft particle in a microchannel

Ji Young Moon,[1] Se Bin Choi,[2] Jung Shin Lee,[2] Roger I. Tanner,[1] and Joon Sang Lee[2,*]
[1]*School of Aerospace, Mechanical and Mechatronic Engineering, The University of Sydney, Sydney, NSW 2006, Australia*
[2]*School of Mechanical Engineering, Yonsei University, Seoul, 03722, Republic of Korea*

(Received 20 March 2018; revised manuscript received 3 July 2018; published 13 February 2019)

Technologies that use optical force to actively control particles in microchannels are a significant area of research interest in various fields. An optical force is generated by the momentum change caused by the refraction and reflection of light, which changes the particle surface as a function of the angle of incidence of light and which in turn feeds back and modifies the force on the particle. Simulating this phenomenon is a complex task. The deformation of a particle, the interaction between the surrounding fluid and the particle, and the reflection and refraction of light should be analyzed simultaneously. Herein, a deformable particle in a microchannel subjected to optical interactions is simulated using the three-dimensional lattice Boltzmann immersed-boundary method. The laser from the optical source is analyzed by dividing it into individual rays. To calculate the optical forces exerted on the particle, the intensity, momentum, and ray direction are calculated. The optical-separator problem with one optical source is analyzed by measuring the distance traveled because of the optical force. The optical-stretcher problem with two optical sources is then studied by analyzing the relation between the intensity of the optical source and particle deformation. This simulation will help the design of sorting and measuring by optical force.

DOI: 10.1103/PhysRevE.99.022607

I. INTRODUCTION

The deformability of cells varies [1–5] and can affect the behavior of cells in circulatory systems. For instance, the deformability of red blood cells (RBCs) is an extremely important determinant of flow because a slight decrease in deformability results in a sharp decrease in capillary flow rate. In severe malaria, RBC deformability is reduced in parasitized RBCs and in uninfected RBCs. Cell deformability is used for cancer diagnosis [4,5]. Circulating tumor cells (CTCs) deform to exit a tumor and enter circulation. Although CTCs are rare in the blood, deformation-based methods for identifying CTCs in patient blood can elucidate the process of cancer metastasis and aid in making informed clinical decisions [6]. Therefore, the measurement of cell deformation and the separation of cells by deformability in a cell papulation are highly relevant for novel clinical investigation, monitoring, and diagnostics [7].

Several techniques have been developed to measure cell deformability. Microfluidic filtration composed by micropore filters was the first method used for measurements of RBC deformability [8]. While the filtration is simple, its disadvantage is to only yield the average information in a cell population or the endpoint information. To measure deformability distributions in a cell population, static single-cell analysis has been introduced. This accurate cell analysis utilizes strain control imposed by suction of a cell in a constriction such as micropipette aspiration [9,10], or by a force exerted with a tip such as cell poker and atomic force microscopy [11–13]. However, these methods have low throughput, which is not applicable to practical situations.

Numerous studies have considered cell separation based on cell size and deformability [14–21]. When a cell suspension containing mouse lymphoma cells (MLCs) and human peripheral blood mononuclear cells (PBMCs) is injected through a two-dimensional (2D) filter array comprising funnel constrictions, PBMCs, which are smaller and more deformable than MLCs, could easily flow through the constrictions, whereas the larger and less deformable MLCs are blocked [19]. When cells from each of eight tumor cell lines are loaded into the device, all cancerous cells are isolated based solely on cell size and deformation characteristics [20]. Inertial focusing is used to manipulate the position and alignment of RBCs within a microchannel; inertial focusing is incorporated into a microfluidic device to isolate and enrich CTCs from diluted blood samples [21]. However, these passive techniques have low purity as well as high fabrication cost, which makes them not suitable for clinical applications.

Nowadays, optical forces, comprising a scattering force pointing in the direction of the light propagation and gradient force acting in the direction of the light-intensity gradient, are used as label-free techniques in a variety of fields [22]. The optical stretcher based on the optical forces has been invented for the measurement of cell deformability distributions in a cell population of cancer cells [23], leukocytes [24–26], or erythrocytes [27–30]. In addition to its capacity of precise control, the optical stretcher has fast and large throughput. Furthermore, the interactions between cells and wall surface that result in cell activation or damage can be ignored in the optical stretching technique [31]. Although the deformability of several cells has been analyzed by the optical stretcher, no standard formula exists yet to explain the relationship between cell deformability and optical forces.

Optical forces can sort biological cells according to several parameters, such as refractive index, size, shape, and

*joonlee@yonsei.ac.kr

fluorescence signal [32–36]. After being aligned in the center of the channel by flow focusing, cells may be analyzed and then switched based on their detected fluorescence [37]. Target cells are then directed by the laser to the collection output, whereas all other cells flow to the waste output. The optical mobility of blood cells tends to increase with cell size because of the radiation force, and the optical mobility of RBCs is larger than the spherical shape cells owing to their biconcave shape [36]. The deformation of the cell membrane can change the magnitude of the optical force exerted on the cell. The dimensionless scattering parameter K (m) represents the conversion efficiency based on the change in photon momentum during the application of the scattering force and tends to be higher for disklike or oval-shaped cells than for spherical cells [37]. This means that the optical mobility of cells should depend on cell deformability when a cell flowing through a microchannel interacts with a laser directed perpendicular to the fluid flow direction. Nevertheless, to our knowledge there is no optical separating technique based on cell deformability. Optical force is generated by the change in momentum that occurs as light refracts and reflects from an interface. Therefore, to analyze the optical force acting on a cell, the refraction and reflection from the cell must be considered in addition to the light intensity. Most microfluidic devices that use other types of active forces can be simulated using a potential to determine the external force as a function of distance between the force source and cells. However, optical force is difficult to describe with such a potential. In the well-known simulation of optical tweezers, optical force is not applied directly to the cell surface but via a light-emitting microbead attached to the cell, thereby generating a constant optical force for cell expansion [38,39]. The microbead is not deformed by the optical force; therefore, a constant force is generated. However, when an optical force targets a cell surface directly, it deforms the cell surface such that the angle of incidence and reflection change, thereby changing the magnitude of the optical force acting on the cell surface. Therefore, even if the same laser is applied, the optical force exerted on the cell surface changes owing to cell deformation.

Numerically interpreting the optical forces acting on floating cells in a fluid is necessary to support, microfluidic channel design, development of the experiments, sorting, and measuring. Solving the optical forces acting on floating cells in a fluid is one of the most challenging and complicated problems in microfluidic science. The complication is arisen by the deformation of cell and interactions with the surrounding fluid. A full description of the floating cell with optical force requires a complete understanding of the interactions between the cell and optical force, interaction between the particles and the matrix fluid, and interactions between channel and particles. Thus, consideration of the above factors can lead to a better understanding of the floating cell with optical force.

In this study, a deformable particle in a microchannel subjected to optical interactions is simulated using the three-dimensional (3D) lattice Boltzmann immersed-boundary method. The results are compared with the experimental data for the validation purpose. In the optical separator problem, a laser is directed perpendicular to the direction of fluid flow so that the optical force shifts deformable cells from their initial fluid streamline to another streamline. To analyze the retention distance and the optical mobility of cells, the effects of cell deformability, flow velocity, and cell size are analyzed. In the optical stretcher problem, the optical forces are generated using two light sources. The cell deforms when it passes through the laser, and the deformation is quantified using the deformation index $\varepsilon(I_D)$. Overall contents and objectives of this paper are shown in Fig. 1.

II. NUMERICAL METHOD

A. Lattice Boltzmann method

The lattice Boltzmann method is widely used to simulate microfluidic flow problems [40,41]. The single-relaxation-time Bhatnagar-Gross-Krook model is used to describe an incompressible fluid. The governing equation with the forcing term is [42]

$$\begin{aligned} f_i(\mathbf{x}+\mathbf{e}_i\Delta t, t+\Delta t) - f_i(\mathbf{x},t) &= -\frac{1}{\tau}\left[f_i(\mathbf{x},t) - f_i^{eq}(\mathbf{x},t)\right] \\ &\quad + \Delta t\left(1-\frac{1}{2\tau}\right)\omega_i\left[\frac{\mathbf{e}_i-\mathbf{u}}{{c_s}^2} + \frac{(\mathbf{e}_i\cdot\mathbf{u})}{{c_s}^4}\mathbf{e}_i\right]\cdot\mathbf{f}, \end{aligned} \quad (1)$$

where the local equilibrium distribution function is

$$f_i^{eq} = \rho\omega_i\left[1 + \frac{1}{{c_s}^2}\mathbf{e}_i\cdot\mathbf{u} + \frac{1}{2{c_s}^4}(\mathbf{e}_i\cdot\mathbf{u})^2 - \frac{1}{2{c_s}^2}\mathbf{u}\cdot\mathbf{u}\right]. \quad (2)$$

For the D3Q19 model,

$$\omega_i = \begin{cases} \frac{1}{3}, & i = 0 \\ \frac{1}{18}, & i = 1, 2, ..., 6 \\ \frac{1}{36}, & i = 7, 8, ..., 18, \end{cases} \quad (3)$$

$$e_i = \begin{cases} (0,0,0) & i = 0 \\ (\pm1,0,0),(0,\pm1,0),(0,0,\pm1) & i = 1, 2, ..., 6 \\ (\pm1,\pm1,0),(\pm1,0,\pm1),(0,\pm1,\pm1) & i = 7, 8, ..., 18. \end{cases} \quad (4)$$

In Eq. (1), the density distribution function $f_i(\mathbf{x},t)$ indicates the fraction of particles moving with lattice velocity i at lattice site $\mathbf{x}$ and time t, Δt is the time step, τ is the particle relaxation time, $\mathbf{e}_i$ is the discrete microscopic velocity, f_i^{eq} is

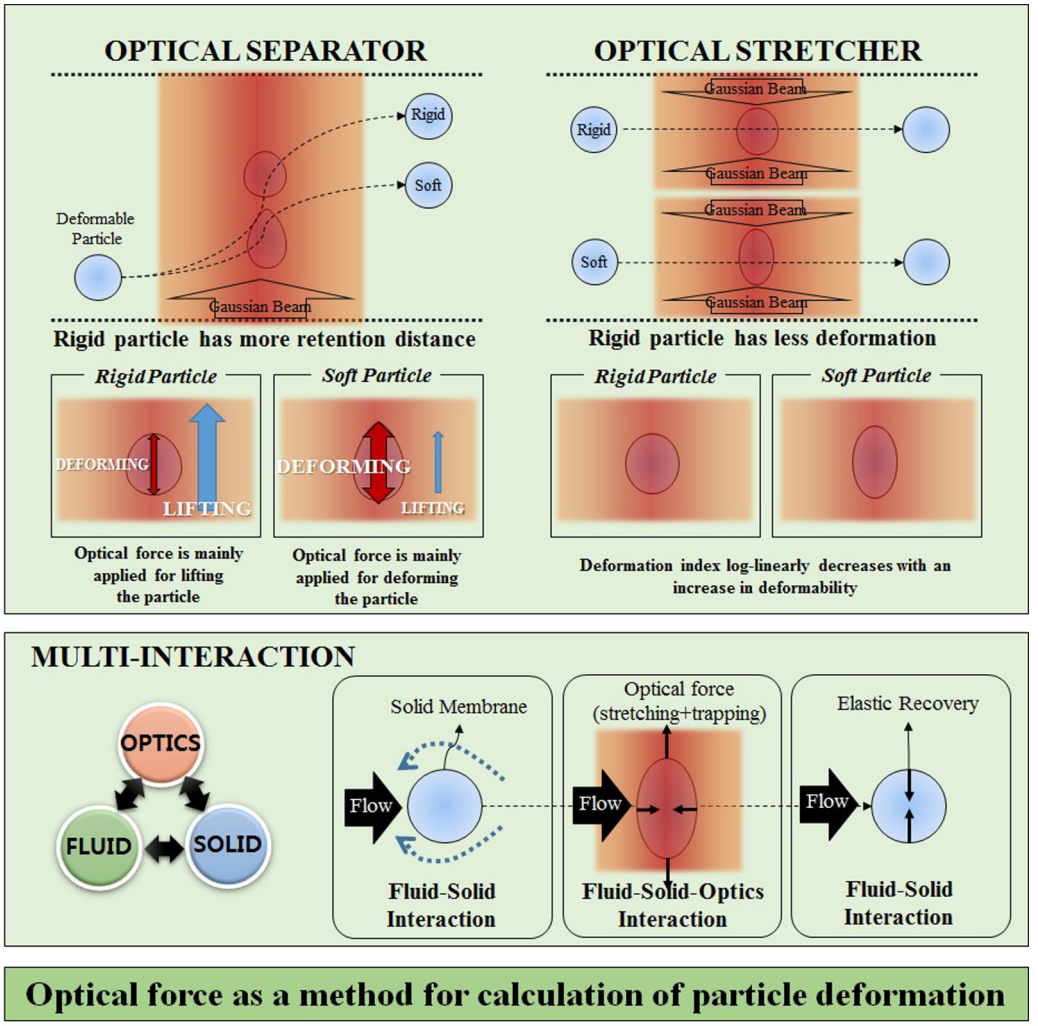

FIG. 1. The objectives of this study are schematically shown. We simulate both optical separator and optical stretcher to analyze the particle deformations. In the optical separator simulations, the more rigid the particle is the more retention distance, because the optical force induced by laser has more dominant effects on lifting force rather than on particle deforming. In the optical stretcher simulations, deformation indices log-linearly decrease as the deformability (shear modulus) increases. Through these simulations, three components—optical force, fluid, and solid—are actively interacted. When the particle starts to move with inlet flow, fluid-solid interaction occurs. In the laser region, the optical force deforms the particle and the deformed particle interacts with the surrounding fluid. After the particle escapes from the laser, the deformed particle is relaxed by elastic recovery and interacts with the surrounding fluid.

the local equilibrium distribution function, and $c_s(=c/\sqrt{3})$ is the speed of sound ($c=\Delta\mathbf{x}/\Delta t$). Fluid density ρ and velocity $\mathbf{u}$ can be calculated using

$$\rho=\sum_i f_i, \quad \rho\mathbf{u}=\sum_i f_i\mathbf{e}_i. \tag{5}$$

The kinematic viscosity is

$$\nu=\left(\tau-\frac{1}{2}\right){c_s}^2\Delta t. \tag{6}$$

Physiologically, a cell is composed of a membrane and cytoplasm. The inner fluid is called the cytoplasm, which contains biomolecules and other proteins. Because of these components, the cytosol is nonlinear viscosity and optically inhomogeneous. The viscosity difference between matrix and cytosol affects the cell deformation and motion. In this study, the cytosol viscosity and matrix viscosity are set to reduce the viscosity difference effect, the scattering and absorption of light at the cell membrane is set to homogeneous to deduce the general, as in many other numerical studies [39,43–46].

B. Three-dimensional deformable-particle mechanics

To simulate cell deformation, a spring-network model is used as shown in Fig. 2. Triangular meshes, which are the most common meshes for simulating the spectrin network of cell membranes, are used. For the constrained spontaneous shape of cells, volume, area, stretching, and bending are used. We use a viscoelastic spring-network model, which accounts for conservation of total volume, dilation of surface area, and bending and stretching of the membrane and mesh density [47–49].

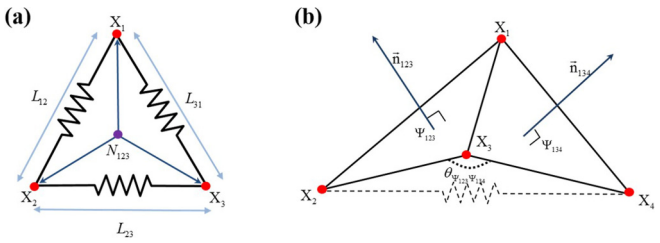

FIG. 2. Spring network of faces Ψ_{123} and Ψ_{134}. (a) L is the distance between Lagrangian nodes. N_{123} is the center of nodes X_1, X_2, and X_3. (b) $\vec{n}$ is the normal vector of face Ψ, and $\theta_{\Psi_{123}\Psi_{134}}$ is the instantaneous angle between faces Ψ_{123} and Ψ_{134}.

The cell membrane is represented by the spring network comprising Lagrangian nodes (see Fig. 2). The stretching force between Lagrangian nodes X_1 and X_2 is

$$F_S(X_1, X_2) = -F_S(X_2, X_1) = -k_S\kappa(\lambda_{12})\Delta L_{12}\vec{L}_{12}\big(\Delta L_{12} = L_{12} - L^0{}_{12}\big), \quad (7)$$

where k_S is the spring constant. The nonlinear (hyperelastic) function κ for neo-Hookean behavior is [50]

$$\kappa(\lambda_{12}) = \frac{(\lambda_{12})^{0.5} + (\lambda_{12})^{-2.5}}{\lambda_{12} + (\lambda_{12})^{-3}}, \quad \left(\lambda_{12} = \frac{L_{12}}{L^0{}_{12}}\right), \quad (8)$$

where L is the instantaneous distance and L_0 is the spontaneous distance between Lagrangian nodes.

The normal vector of face Ψ_{123} is

$$\vec{n}_{123} = (X_2 - X_1) \times (X_3 - X_1)/|(X_2 - X_1) \times (X_3 - X_1)|. \quad (9)$$

The center of the plane is

$$N_{123} = \frac{(X_1 + X_2 + X_3)}{3}. \quad (10)$$

The bending force between faces Ψ_{123} and Ψ_{134} is

$$F_B(X_2)/\vec{n}_{123} = F_B(X_4)/\vec{n}_{134} = -k_B\big[1 - \cos\big(\theta_{\Psi_{123}\Psi_{134}} - \theta^0{}_{\Psi_{123}\Psi_{134}}\big)\big], \quad (11)$$

$$\theta_{\Psi_{123}\Psi_{134}} = \pi - \cos^{-1}(\vec{n}_{123} \cdot \vec{n}_{123}) \text{ when } c_{\Psi_{123}\Psi_{134}} \leqslant 0$$

otherwise,

$$\theta_{\Psi_{123}\Psi_{134}} = \pi + \cos^{-1}(\vec{n}_{123} \cdot \vec{n}_{123}), \quad (12)$$

$$c_{\Psi_{123}\Psi_{134}} = (N_{123} - N_{134}) \cdot \vec{n}_{123}, \quad (13)$$

$$F_B(X_3) = F_B(X_3) = \frac{F_B(X_2) + F_B(X_4)}{2}, \quad (14)$$

where k_B is the bending constant, θ is the instantaneous angle, and θ_0 is the spontaneous angle. $c_{\Psi\Psi}$ is the angle indicator, which determines whether the angle is obtuse or acute. To simulate the deformation, the spring energy relating a single-triangle face to the overall energy is

$$E_{\mathrm{AL}}(\Psi_{123}) = k_{\mathrm{AL}}\frac{[\Delta A(\Psi_{123})]^2}{2A(\Psi_{123})}. \quad (15)$$

Similarly, the volume energy can be expressed as [48]

$$E_V(\Psi_{123}) = -k_V\frac{(V - V_0)^2}{V_0}\vec{n}_{123}. \quad (16)$$

The spring-network model used in this study is a simplified alternative to the energy model. The constraints of conservation of area and volume yield [49,51]

$$F_A(\Psi_{123}, X_1) = F_{\mathrm{AL}}(\Psi_{123}, X_1) + F_{\mathrm{AG}}(\Psi_{123}, X_1) = -\left(k_{\mathrm{AL}}\frac{\Delta A(\Psi_{123})}{\sqrt{A(\Psi_{123})}} + k_{\mathrm{AG}}\frac{\Delta A_T}{A_T}\right)(X_1 - N_{123}), \quad (17)$$

$$A(\Psi_{123}) = [(X_2 - X_1) \times (X_3 - X_1)]/2, \quad (18)$$

$$F_V(\Psi_{123}, X_1) = -k_V\frac{V - V_0}{3V_0}A(\Psi_{123})\vec{n}_{123}, \quad (19)$$

$$V = \sum_{\Psi}(N \cdot \vec{n})A(\Psi)/3, \quad (20)$$

where k_{AL}, k_{AG}, and k_V are the local-area-, global-area-, and volume-constraint constants, respectively. The quantities A_T, V, and V_0 are the total area, instantaneous total volume, and spontaneous total volume, respectively. The total elastic force under given the constrained spontaneous shape is

$$F = F_V + F_A + F_S + F_B. \quad (21)$$

C. Optical force

To calculate the optical forces acting on a cell, the intensity, momentum, and direction of the laser are calculated by dividing it into individual rays. Refraction and reflection are calculated for each ray based on the normal vector at the cell surface. The ray optics approach is valid when the object is much larger than the wavelength of the light. For spherical objects, the condition is given as $2\pi a/\lambda \gg 1$, where a is the radius of the sphere and λ is the laser wavelength. The radius of the soft particles that we used in this study is greater than 9 μm and the laser wavelength is less than 1 μm, so the condition was satisfied [52]. The optical force resulting from the change in momentum of an individual ray is depicted in Fig. 3.

The difference in momentum between the incident ray and the refracted and reflected rays is used to calculate the optical force, which yields

$$\overrightarrow{R_1} = -(\overrightarrow{p_1} + |\overrightarrow{p_1} \cdot \overrightarrow{n}|\overrightarrow{n}), \quad (22)$$

$$\overrightarrow{R_2} = -\overrightarrow{R_1}\frac{n_1}{n_2}, \quad (23)$$

$$\overrightarrow{p_2} = \overrightarrow{R_2} - \overrightarrow{n}\sqrt{|\overrightarrow{p_1}|^2 - |\overrightarrow{R_2}|^2}, \quad (24)$$

$$\overrightarrow{F} = -c(\overrightarrow{p_2} - \overrightarrow{p_1}), \quad (25)$$

where $\overrightarrow{p}$ is the momentum of the individual ray, n is the index of refraction, and c is a constant relating momentum to force. The refractive index for the fluid is $n_1 = 1.33$ and for the cell, $n_2 = 1.4$. We assume that Fresnel coefficient is 0.

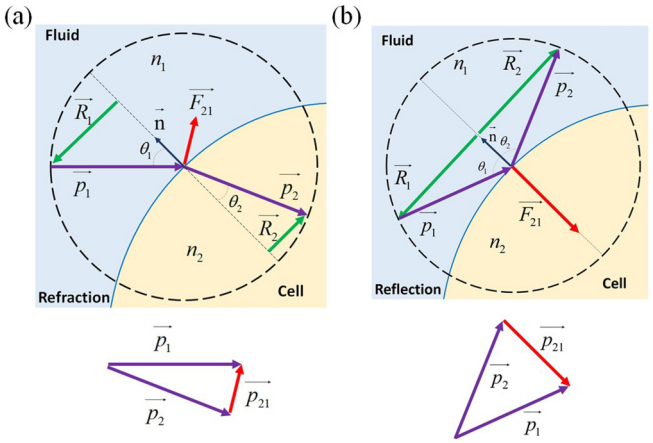

FIG. 3. Optical force generated by change in momentum of individual ray owing to (a) refraction and (b) reflection.

We calculated the laser by dividing it into rays of Cartesian mesh type at regular intervals. The intensity of the rays follows the Gaussian distribution where the intensity becomes stronger toward the center of the laser.

The momentum of each ray is

$$p = nE/c_l, \tag{26}$$

where E is the energy of the ray and c_l is the speed of light in vacuum [53,54]. The optical force obtained is summed with the elastic force [Eq. (21)].

D. Lattice Boltzmann immersed-boundary method

We use the immersed-boundary method to determine the interaction between the fluid and cells [55–57]:

$$\mathrm{f}(\mathbf{x}, t) = \int D[\mathbf{x} - \mathbf{X}(\mathbf{s}, t)]\mathrm{F}(\mathbf{s}, t)d\mathbf{s}, \tag{27}$$

$$\frac{\partial \mathbf{X}(\mathbf{s}, t)}{\partial t} = \mathbf{u}[\mathbf{x}(\mathbf{s}, t), t] = \int \mathbf{u}(\mathbf{x}, t)D[\mathbf{x} - \mathbf{X}(\mathbf{s}, t)]d\mathrm{x}, \tag{28}$$

$$D(\mathbf{x} - \mathbf{X}(\mathbf{s}, t)) = \frac{1}{64h^3}\left[1 + \cos\left(\frac{\pi x}{2h}\right)\right]\left[1 + \cos\left(\frac{\pi y}{2h}\right)\right]\left[1 + \cos\left(\frac{\pi z}{2h}\right)\right]_{\text{for } D3Q19}$$
$$\text{when } |x \text{ and } y \text{ and } z| \leqslant 2h, \quad \text{otherwise } D(\mathbf{x}) = 0, \tag{29}$$

where $\mathbf{f}$, $\mathbf{x}$, and $\mathbf{u}$ are the force density acting on the fluid node, Eulerian coordinates, and fluid velocity, respectively, and $\mathbf{X}$ and $\mathbf{F}$ are the Lagrangian coordinates and restoring force density of the cell, respectively. D is the Dirac δ function for interpolation. Equations (27) and (28) represent the immersed-boundary equation for communication between Eulerian and Lagrangian coordinates. The unknown quantities are the force per unit volume $\mathrm{f}(\mathbf{x}, t)$, applied by the immersed boundary in the fluid, and the velocity of each Lagrangian node, $\mathbf{u}[\mathbf{X}(\mathbf{s}, t), t]$. Equation (27) describes the force density $\mathbf{f}(\mathbf{x}, t)$ of the fluid calculated from the Lagrangian restoration of the elastic force density, $\mathbf{F}(\mathbf{s}, t)$, via interpolation over the immersed boundary. Equation (28) assumes that the no-slip boundary condition is applied to the membrane because the Lagrangian nodes move at the same velocity as the surrounding fluid. Equation (29) uses the 3D Dirac δ function $D[\mathbf{x} - \mathbf{X}(\mathbf{s}, t)]$, which relates the interactions between Eulerian coordinates (fluid nodes) and Lagrangian coordinates (deformable-particle boundary nodes).

III. RESULTS

A. Simulation overview

Figure 4 shows the snapshots of the simulation domain for simulating an optical stretcher and optical separator. The sphere models the geometry of a cell. The laser cross-sectional area is $100 \times 20\ \mu\mathrm{m}^2$ for the optical separator and $4 \times 4\ \mu\mathrm{m}^2$ for the optical stretcher. The power of the laser is normally distributed about the laser center. For the optical separator, the laser irradiates from a single side, and the optical stretcher is placed on both sides of the laser. The body force F_P is summed over all fluid nodes to determine the pressure-gradient-driven flow. The pressure gradient is a function of L:

$$\Delta p = \rho L F_P, \tag{30}$$

where L is the length of the computational domain.

For this study, the viscosity and the density of the fluid are $\mu = 10^{-3}$ Pa s and $\rho = 1000\ \mathrm{kg/m^3}$. The stretching constant k_S and area-dilation constant k_{AL} for most deformable-solid simulations are based on a continuum model, which is determined by the shear modulus $G_s = \sqrt{3}k_S/4$ and Young's modulus $E = 2k_S/\sqrt{3}$ [58]. For the sake of simplicity and generality, the dimensionality of the constant elasticity is reduced using the ratio between the bending forces and in-plane stretching forces. The ratio of the bending force to the stretching force may be approximated as $\xi \approx k_B/(R^2k_S) = O(10^{-3})$ [46,59]. Similarly, the dilation modulus can be approximated as $k_A/k_S \approx 2.0$.

B. Optical separator

To validate the proposed model, the retention distance of each cell component is measured using 3 W of laser power and various white blood cells: lymphocytes, granulocytes, and monocytes, which have different cell sizes. The retention distance is calculated by measuring the position of the cell just before passing through the laser and the change in the cell's vertical position after passing through the laser. The results shown in Fig. 5 indicate that the retention distance increases with cell sizes. The optical force is larger for larger cells because of the growth of the membrane area over which the optical force is exerted. Flow velocity also affects retention distance. A high inertial force caused by high flow velocity

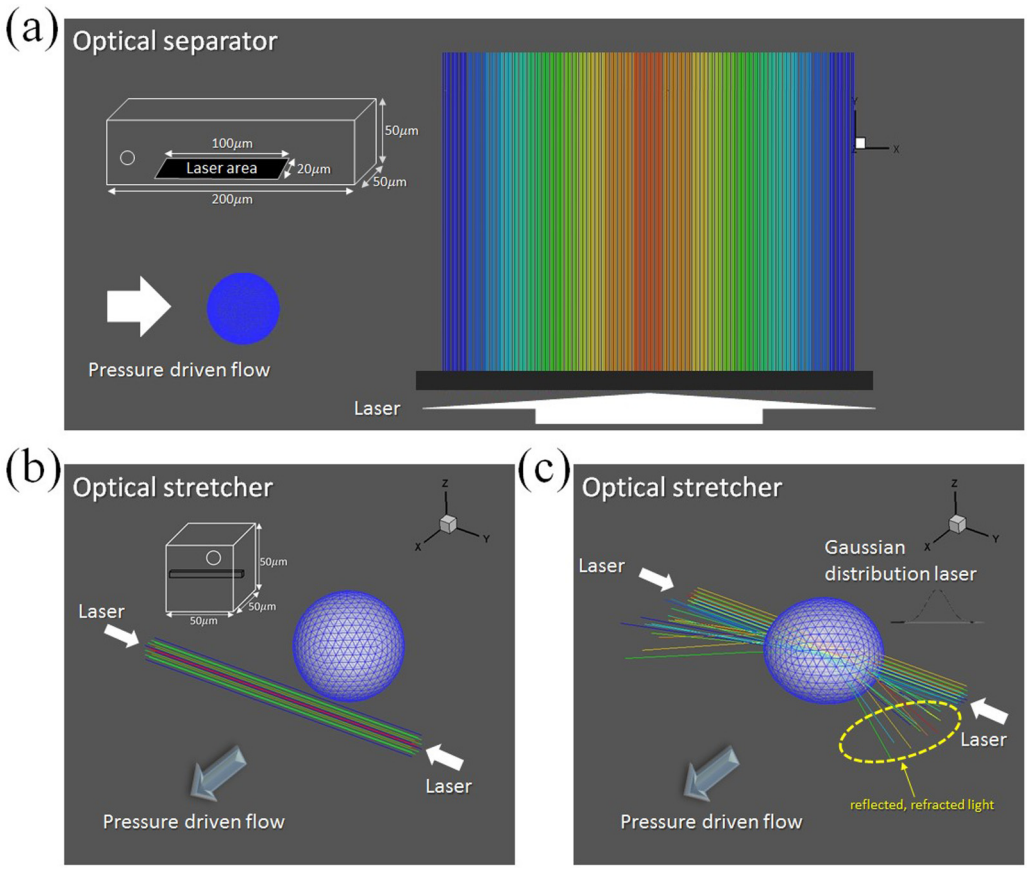

FIG. 4. Snapshots of domain are used for simulating an optical stretcher and optical separator. The laser is normally distributed about the laser center. For the optical stretcher, the laser is irradiated from both sides. For the optical separator, the laser is irradiated from a single side. (a) Initial condition of optical-separator simulation. (b) Initial condition of optical-stretcher simulation. (c) Snapshot showing the cell passing through a laser at $G_s = 25\,\mu$N/m, 1 W.

drives the cells quickly through the laser so that the retention distance decreases with increasing flow velocity.

To understand the effect of both cell size and flow velocity on the retention distance, we use the concept of optical

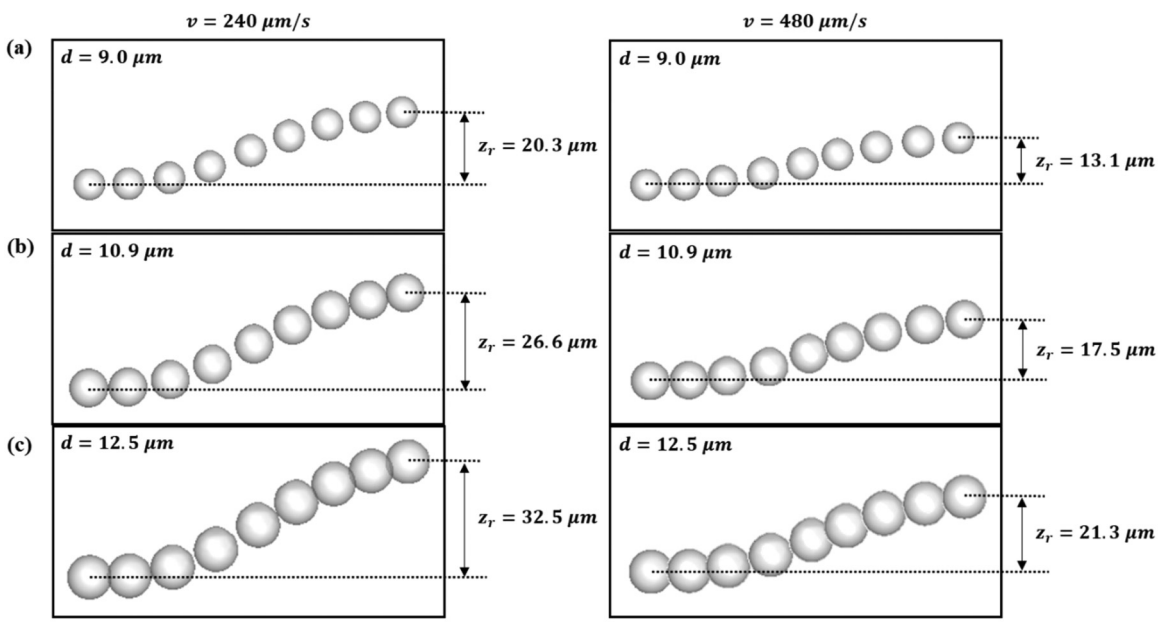

FIG. 5. Change in retention distance for different cells: (a) lymphocytes, (b) granulocytes, and (c) monocytes.

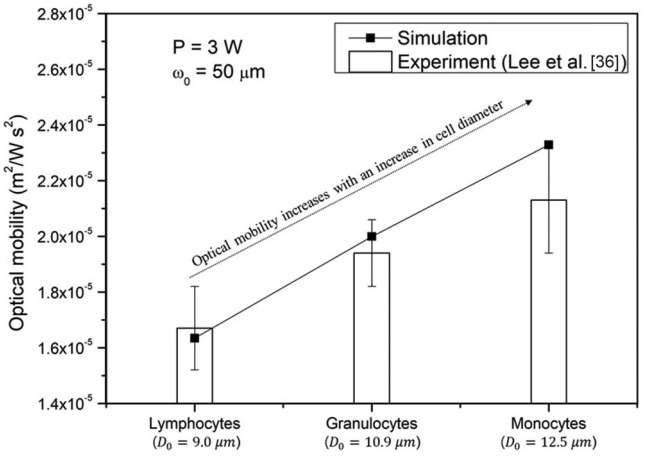

FIG. 6. Experimentally determined optical mobility of lymphocytes, granulocytes, and monocytes for optical separator (data points with error bars) compared with the results of simulation (histogram bars).

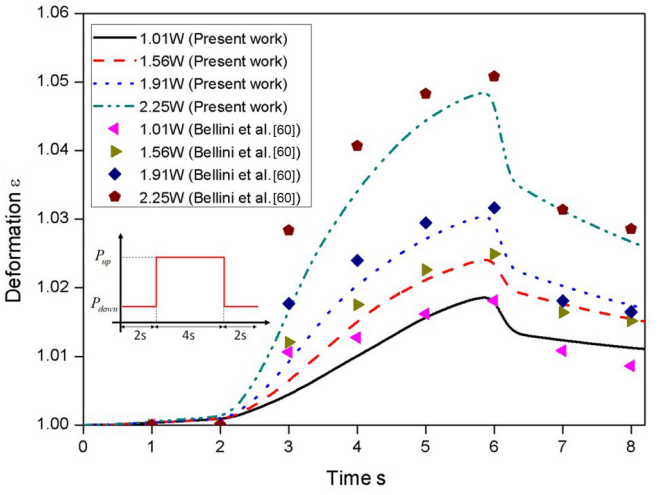

FIG. 8. Comparison of HL60 response to step-like increase in applied optical power between experimental results [60] and numerical results in this paper.

mobility, which is expressed as

$$z_{\text{opt}} = z_z\left(\frac{cu\omega_0}{2n_1P}\right), \tag{31}$$

where u is the flow velocity, ω_0 is the waist of the laser, n_1 is the index of refraction of the medium, and P is the laser power. The optical mobility expresses the relation between cell, laser, and flow. Calculating the optical mobility allows the effect of cell size and flow velocity to be normalized. Figure 6 shows the optical mobility for different cells and shows that the optical mobility increases with cell diameter. The results of the simulation are consistent with experimental results [36].

Figure 7(a) shows that the retention distance depends on shear modulus. The retention distance gradually increases with shear modulus at all particle sizes. To investigate how the retention distance depends on shear modulus, we calculate the optical force applied in the y direction (perpendicular to the flow). As shown in Fig. 7(b), the optical force that increases with shear modulus provides a good prediction of the relation between retention distance and shear modulus. The optical force depends on many variables, such as cell shape, position, and cell-flow interaction. The resulting hydrodynamic force decreases with increasing shear modulus because of drag, which is influenced by cell deformation. When the laser is projected onto the cell membrane, the cell is deformed into an elliptical shape, which reduces drag. In turn, the reduced drag leads to a larger hydrodynamic force. Therefore, softer particles with low shear moduli are deformed more into elliptical shapes and are lifted higher because of reduced drag. However, the hydrodynamic force is much smaller than the optical force, which means that hydrodynamic contributions on the retention distance can be ignored. Instead, the deformability of particles has a significant effect on the retention distance. The optical energy has contributions to the deformation of soft particle and the retention distance. For softer particles, the optical energy has more contributions to the deformation of the particles rather

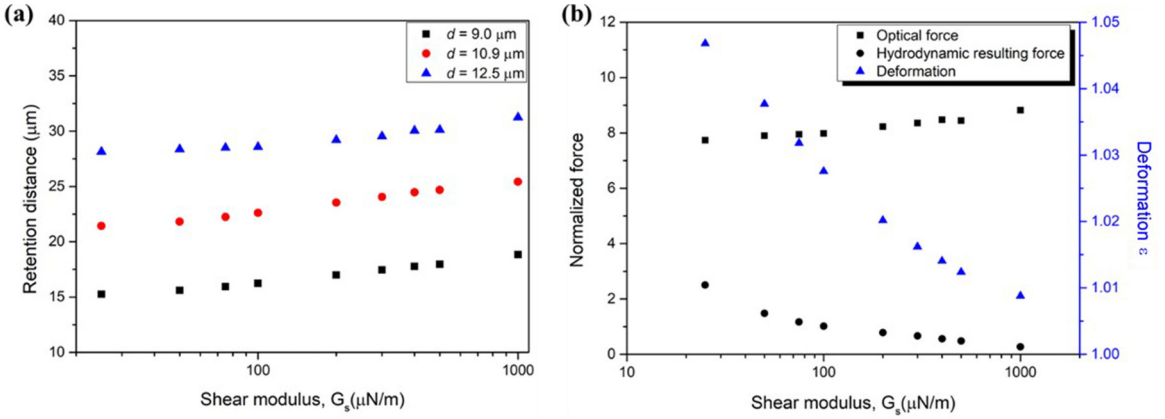

FIG. 7. (a) Retention distance as a function of shear modulus at different particle size. At all range of shear modulus, the retention distance is proportional to shear modulus. (b) Normalized force applied in y direction (perpendicular to flow) and time-averaged deformation as a function of shear modulus.

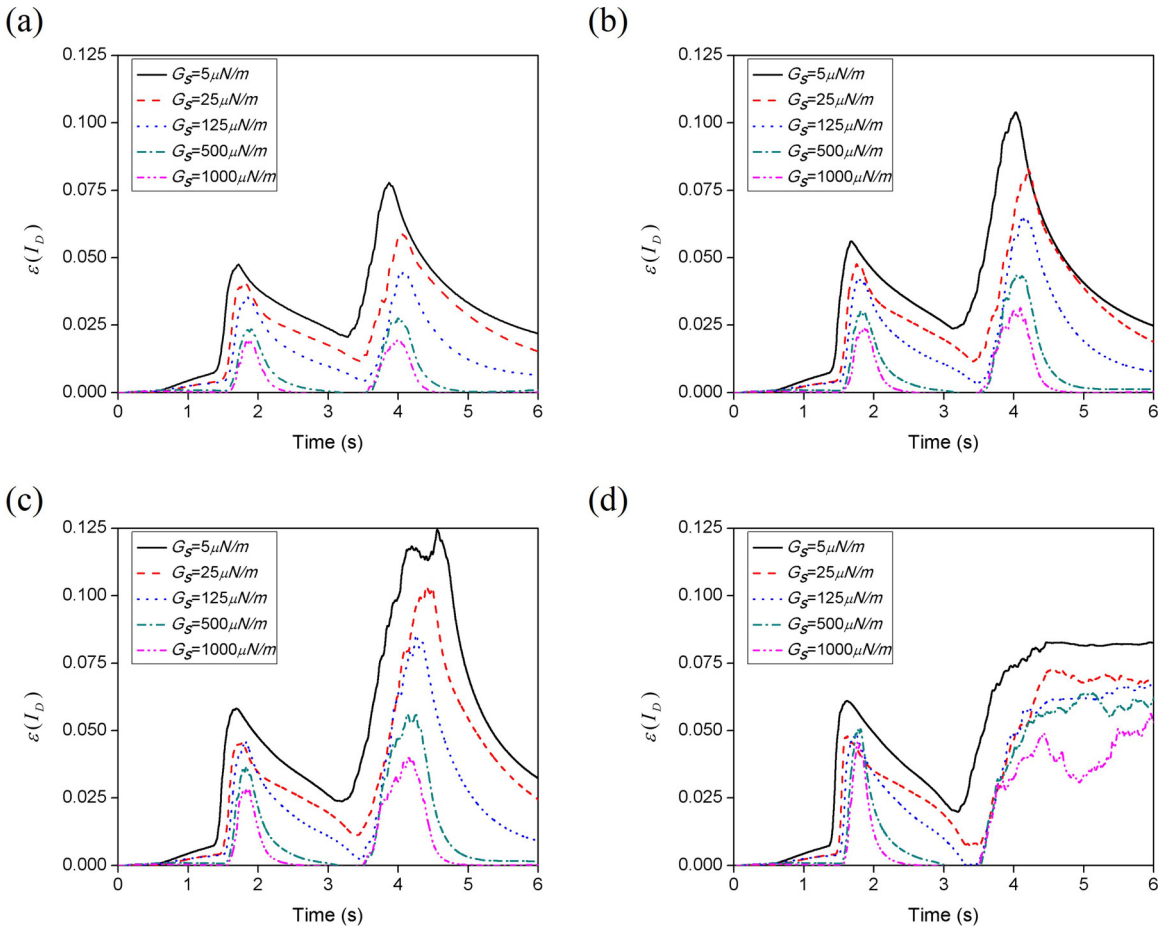

FIG. 9. Deformation index $\varepsilon(I_D)$ changes as a function of the time for different laser power: (a) 1, (b) 1.5, (c) 2 W, and (d) 4W. In all cases, two peaks typically appear.

than the retention distance. On the contrary to this, the optical energy has more contributions to the retention distance for more rigid particles.

C. Optical stretcher

The numerical results of a deformable cell with optical force is compared with the optical stretcher experiment for the validation purpose [60]. Figure 8 shows the comparison between our results, and experiment data. For this procedure, the numerical experiment of optical stretcher was set with the following values for HL60: $E = 2675$ Pa [61]. HL60 is a cell line of human promyelocytic leukemic. Optical stretching simulations are performed by applying a steplike laser power increase to the HL60 cell. Stretching experiments are performed by applying a steplike laser power increase to the HL60 cells. When the cell is stationary, $P_{\text{down}} = 180$ mW applied for 2 s, the steplike stimulus increase the power to a value P_{up} for 4 s, finally the power is decreased to the same initial P_{down} for 2 s. We calculated deformation ε and deformation index $\varepsilon(I_D)$ computed by the following formula:

$$\varepsilon = \frac{a}{a_0}, \tag{32}$$

$$\varepsilon(I_D) = \frac{a-b}{a+b}, \tag{33}$$

where a and b are the laser axis and flow axis of the cell size during the stretching process, respectively. a_0 is initial size of cell.

Figure 9 shows $\varepsilon(I_D)$ as a function of time for five different shear moduli of cells (5, 25, 125, 500, and 1000 μN/m). Four laser powers (1, 1.5, 2, and 4 W) are used to pull and stretch the cells. As a cell passes through the lase, two peaks appear in $\varepsilon(I_D)$. Cell size is 10 μm in all cases. The first peak occurs when the cell first interacts with the laser, and the second peak appears just before the cell leaves the optical force trap generated by the laser. As P increases, $\varepsilon(I_D)$ peaks become larger, and the time taken until the second peak occurred after the first peak occurred increased. When P is 4 W, the cells could not pass and were trapped.

In general, as P increases, the transverse diameter of the cell becomes greater than the axial diameter; therefore, $\varepsilon(I_D)$ increases. Despite the increasing power of the laser, the height of the first peak change is relatively small, irrespective of P: when laser strikes the cell, the cell is pulled toward the laser and is trapped. $\varepsilon(I_D)$ difference between the first and second peaks decreased as the deformability of the cells decreased. The time difference between the first peak and the second peak increases with the trap effect as P increases.

We now derive the relation between $\varepsilon(I_D)$ for the optical stretcher and cell deformability by analyzing the trends of the

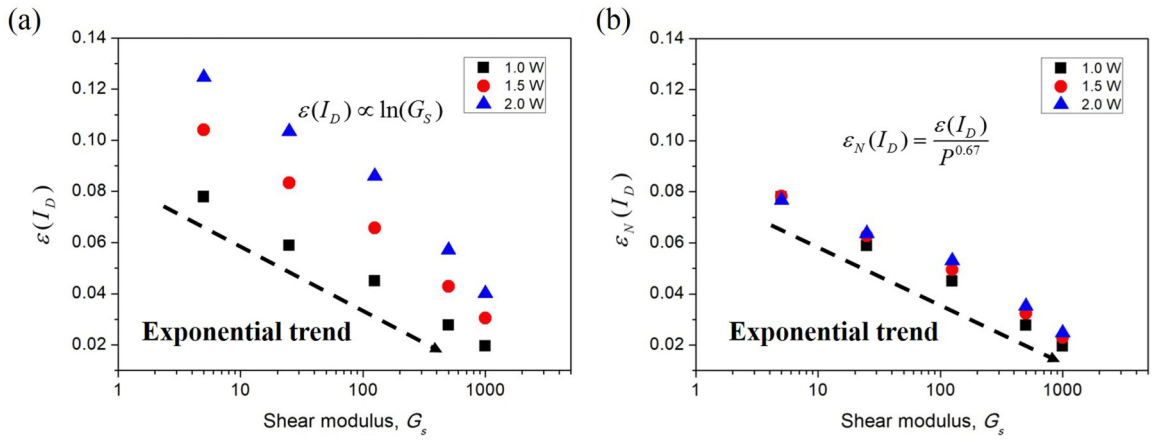

FIG. 10. (a) Deformation index $\varepsilon(I_D)$ and (b) normalized deformation index $\varepsilon_N(I_D)$ for different laser power P as a function of the shear modulus at second peak in Fig. 9.

two peak heights in Fig. 9, which are because of the cells passing through the optical stretcher. No tendency is found for the first peak, but one is found in the second peak. Figure 10 shows $\varepsilon(I_D)$ and normalized deformation index $\varepsilon_N(I_D)$ from the second peak as a function of shear modulus of the cell and for several laser powers. In terms of the shear modulus, $\varepsilon(I_D)$ can be expressed as $\varepsilon(I_D) \propto \ln(G_s)$. To generalize this, $\varepsilon(I_D)$ is normalized to P, which provides

$$\varepsilon_N(I_D) = \frac{\varepsilon(I_D)}{P^{0.67}} = \frac{a \ln(G_s)}{P^{0.67}}, \tag{34}$$

where a is constant. The shear modulus is

$$G_s = e^{\varepsilon_N(I_D) \times P^{0.67}/a}. \tag{35}$$

Equation (35) expresses the relation between shear modulus, $\varepsilon(I_D)$, and P. A more accurate relation may be obtained by adjusting the above equations based on more experimental results and simulations that consider fluid conditions.

IV. CONCLUSIONS

This study analyzes cell deformation and soft particle behavior caused by optical forces in pressure-driven flow. In a Cartesian mesh, we use the lattice Boltzmann method to analyze the fluid and an unstructured moving mesh to analyze particle deformation. The laser is modeled as rays, and the optical force is calculated from the change in momentum caused by refraction and reflection. Optical and hydrodynamic forces generated by the surrounding fluid deforms the particle, which modifies the degree of refraction and of refraction of the ray, thereby changing the hydrodynamic force exerted on the particle. The simulation accounts for the three-way coupling among laser, particle, and fluid.

To simulate optical separation, an optical force is generated using only a single laser source. This optical force moves the particle to the opposite side of the light source, and the retention distance, which is the distance the particle moves, depends on the particle characteristics. For shear modulus, the retention distance is inversely proportional to the shear modulus. For an optical stretcher, the optical forces are generated using two laser sources. The particle deforms when it passes through the laser, and the deformation is quantified using $\varepsilon(I_D)$. $\varepsilon(I_D)$ peaks show exponential decay as a function of shear modulus as the particle passes through the optical stretcher, and we derive a relation between the deformation and the particle properties based on the second peak. This study will help design and optimize microfluidic devices using optical forces.

ACKNOWLEDGMENTS

This work was supported by the Advanced Research Center Program (Grant No. NRF-2015R1A5A1037668) through a National Research Foundation of Korea (NRF) grant funded by the Ministry of Science, ICT, and Future Planning (MSIP).

[1] S. Chien, Annu. Rev. Physiol. **49**, 177 (1987).
[2] M. J. Rosenbluth, W. A. Lam, and D. A. Fletcher, Biophys. J. **90**, 2994 (2006).
[3] S. C. Tan, W. X. Pan, G. Ma, N. Cai, K. W. Leong, and K. Liao, BMC Cell Biol. **9**, 40 (2008).
[4] A. M. Dondorp, B. J. Angus, K. Chotivanich, K. Silamut, R. Ruangveerayuth, M. R. Hardeman, P. A. Kager, J. Vreeken, and N. J. White, J. Trop. Med. Hyg. **60**, 733 (1999).
[5] W. Zhang, K. Kai, D. S. Choi, T. Iwamoto, Y. H. Nguyen, H. Wong, M. D. Landis, N. T. Ueno, J. Chang, and L. Qin, Proc. Natl. Acad. Sci. U.S.A. **109**, 18707 (2012).
[6] J. S. Bagnall, S. Byun, S. Begum, D. T. Miyamoto, V. C. Hecht, S. Maheswaran, S. L. Stott, M. Toner, R. O. Hynes, and S. R. Manalis, Sci. Rep. **5**, 18542 (2015).
[7] P. Preira, V. Grandne, J.-M. Forel, S. Gabriele, M. Camara, and O. Theodoly, Lab. Chip. **13**, 161 (2013).

[8] H. Reid, A. Barnes, P. Lock, J. Dormandy, and T. Dormandy, J. Clin. Pathol. **29**, 855 (1976).

[9] A. T. Skoutelis, V. E. Kaleridis, G. M. Athanassiou, K. I. Kokkinis, Y. F. Missirlis, and H. P. Bassaris, Crit. Care Med. **28**, 2355 (2000).

[10] A. T. Skoutelis, V. E. Kaleridis, C. A. Gogos, G. M. Athanassiou, Y. F. Missirlis, and H. P. Bassaris, Cytokine **12**, 1737 (2000).

[11] F. Lautenschläger, S. Paschke, S. Schinkinger, A. Bruel, M. Beil, and J. Guck, Proc. Natl. Acad. Sci. U.S.A. **106**, 15696 (2009).

[12] G. Worthen, B. Schwab, E. Elson, and G. Downey, Science **245**, 183 (1989).

[13] W. A. Lam, M. J. Rosenbluth, and D. A. Fletcher, Blood **109**, 3505 (2007).

[14] Z. T. F. Yu, K. M. Aw Yong, and J. Fu, Small **10**, 1687 (2014).

[15] S. H. Seal, Cancer **17**, 637 (1964).

[16] H. W. Hou, M. E. Warkiani, B. L. Khoo, Z. R. Li, R. A. Soo, D. S. W. Tan, W. T. Lim, J. Han, A. A. S. Bhagat, and C. T. Lim, Sci. Rep. **3**, 1259 (2013).

[17] S. Zheng, H. Lin, J. Q. Liu, M. Balic, R. Datar, R. J. Cote, and Y. C. Tai, J. Chromatogr. A. **1162**, 154 (2007).

[18] S. C. Hur, N. K. Henderson-MacLennan, E. R. McCabe, and D. Di Carlo, Lab. Chip. **11**, 912 (2011).

[19] S. M. McFaul, B. K. Lin, and H. Ma, Lab. Chip. **12**, 2369 (2012).

[20] H. Mohamed, M. Murray, J. N. Turner, and M. Caggana, J. Chromatogr. A **1216**, 8289 (2009).

[21] N. M. Karabacak, P. S. Spuhler, F. Fachin, E. J. Lim, V. Pai, E. Ozkumur, J. M. Martel, N. Kojic, K. Smith, P. I. Chen, and J. Yang, Nat. Protoc. **9**, 694 (2014).

[22] F. Schaal, M. Warber, S. Zwick, H. van der Kuip, T. Haist, and W. Osten, J. Eur. Opt. Soc. **4**, 09028 (2009).

[23] G. B. Nash, B. Christopher, A. J. Morris, and J. A. Dormandy, Heart **62**, 329 (1989).

[24] P. Preira, T. Leoni, M.-P. Valignat, A. Lellouch, P. Robert, J.-M. Forel, L. Papazian, G. Dumenil, P. Bongrand, and O. Théodoly, Int. J. Nanotechnol. **9**, 529 (2012).

[25] M. J. Rosenbluth, W. A. Lam, and D. A. Fletcher, Lab Chip **8**, 1062 (2008).

[26] S. Gabriele, A. Benoliel-M., P. Bongrand, and O. Théodoly, Biophys. J. **96**, 4308 (2009).

[27] M. Abkarian, M. Faivre, and H. Stone, Proc. Natl. Acad. Sci. U.S.A. **103**, 538 (2006).

[28] T. Herricks, M. Antia, and P. K. Rathod, Cell. Microbiol. **11**, 1340 (2009).

[29] S. Shevkoplyas, T. Yoshida, S. Gifford, and M. Bitensky, Lab. Chip. **6**, 914 (2006).

[30] Q. Guo, S. J. Reiling, P. Rohrbach, and H. Ma, Lab. Chip. **12**, 1143 (2012).

[31] T. W. Kuijpers, A. T. Tool, C. E. van der Schoot, L. A. Ginsel, J. J. Onderwater, D. Roos, and A. J. Verhoeven, Blood **78**, 1105 (1991).

[32] K. Ladavac, K. Kasza, and D. G. Grier, Phys. Rev. E **70**, 010901 (2004).

[33] M. M. Wang, E. Tu, D. E. Raymond, J. M. Yang, H. Zhang, N. Hagen, B. Dees, E. M. Mercer, A. H. Forster, I. Kariv, and P. J. Marchand, Nat. Biotechnol. **23**, 83 (2005).

[34] A. A. S. Bhagat, H. Bow, H. W. Hou, S. J. Tan, J. Han, and C. T. Lim, Med. Biol. Eng. Comput. **48**, 999 (2010).

[35] I. Sraj, C. D. Eggleton, R. Jimenez, E. E. Hoover, J. A. Squier, J. Chichester, and D. W. Marr, J. Biomed. Opt. **15**, 047010 (2010).

[36] K. Heon Lee, K. Soo Lee, J. Ho Jung, C. Bong Chang, and H. Jin Sung, Appl. Phys. Lett. **102**, 141911 (2013).

[37] S. J. Hart, A. Terray, T. A. Leski, J. Arnold, and R. Stroud, Anal. Chem. **78**, 3221 (2006).

[38] M. Dao, C. T. Lim, and S. Suresh, J. Mech. Phys. Solids **51**, 2259 (2013).

[39] D. A. Fedosov, B. Caswell, and G. E. Karniadakis, Biophys. J. **98**, 2215 (2010).

[40] J. Y. Moon, S. Kondaraju, W. Choi, and J. S. Lee, Microfluid. Nanofluid. **17**, 1061 (2014).

[41] J. Y. Moon, R. I. Tanner, and J. S. Lee, Biomicrofluidics. **10**, 044110 (2016).

[42] Z. Guo, C. Zheng, and B. Shi, Phys. Rev. E **65**, 046308 (2002).

[43] P. B. Bareil, Y. Sheng, Y. Q. Chen, and A. Chiou, Opt. Express **15**, 16029 (2007).

[44] P. B. Bareil, Y. Sheng, and A. E. Chiou, Proc. SPIE **7400**, 74000D (2009).

[45] Y. Imai, H. Kondo, T. Ishikawa, C. T. Lim, and T. Yamaguchi, Biomechanics **43**, 1386 (2010).

[46] T. Wu and J. J. Feng, Biomicrofluidics **7**, 044115 (2013).

[47] M. M. Dupin, I. Halliday, C. M. Care, L. Alboul, and L. L. Munn, Phys. Rev. E. **75**, 066707 (2007).

[48] M. Nakamura, S. Bessho, and S. Wada, Int. J. Numer. Method. Biomed. Eng. **29**, 114 (2013).

[49] I. Jančigová and I. Cimrák, Int. J. Numer. Method. Biomed. Eng. **32**, e02757 (2016).

[50] J. Dupire, M. Socol, and A. Viallat, Proc. Natl. Acad. Sci. U.S.A. **109**, 20808 (2012).

[51] I. Jančigová and R. Tóthová, Scalability of forces in mesh-based models of elastic objects, *ELEKTRO 2014: 10th International Conference, Rajecke Teplice, Slovakia* (IEEE, 2014), pp. 562–566.

[52] J. Guck, R. Ananthakrishnan, H. Mahmood, T. J. Moon, C. C. Cunningham, and J. Käs, Biophys. J. **81**, 767 (2001).

[53] A. Ashkin and J. M. Dziedzic, Phys. Rev. Lett. **30**, 139 (1973).

[54] I. Brevik, Phys. Rep. **52**, 133 (1979).

[55] C. S. Peskin, Acta Numer. **11**, 479 (2002).

[56] C. Pozrikidis, J. Fluid Mech. **440**, 269 (2001).

[57] Z. G. Feng and E. E. Michaelides, J. Comput. Phys. **195**, 602 (2004).

[58] H. S. Seung and D. R. Nelson, Phys. Rev. A **38**, 1005 (1988).

[59] T. Krüger, B. Kaoui, and J. Harting, J. Fluid Mech. **751**, 725 (2014).

[60] N. Bellini, F. Bragheri, I. Cristiani, J. Guck, R. Osellame, and G. Whyte, Biomed. Opt. Express **3**, 2658 (2012).

[61] P. Sajeesh, A. Raj, M. Doble, and A. K. Sen, RSC Adv. **6**, 74704 (2016).